J. Korean Soc. Ind. Appl. Math. Vol.29, No.4, 377–388, 2025 https://doi.org/10.12941/jksiam.2025.29.377

THE ALLEN–CAHN EQUATION WITH DOMAIN-DEPENDENT FREE ENERGY

SEONGHO SHIN [1] AND DONGSUN LEE[1,2†]

[1]DEPARTMENT OF MATHEMATICS EDUCATION, INCHEON NATIONAL UNIVERSITY, INCHEON 21999, REPUBLIC OF KOREA

[2]RESEARCH CENTER FOR BIO MATERIALS & PROCESS DEVELOPMENT, INCHEON NATIONAL UNIVERSITY, INCHEON 22012, REPUBLIC OF KOREA

Email address: shinsh6187@inu.ac.kr, [†]esen@inu.ac.kr

ABSTRACT. This study presents a numerical investigation of the Allen–Cahn equation incorporating a domain-dependent free energy functional. We adopt a quartic polynomial potential to approximate the logarithmic free energy, effectively capturing the thermodynamic characteristics of phase separation while maintaining analytical tractability. Through three-dimensional numerical simulations, we analyze the morphological evolution of the phase field under spatially varying temperature parameters, θ_1. A comparative analysis of three distinct cases reveals that a marginal difference of 0.02 in the maximum value of θ_1 is sufficient to induce distinctly different final topological states, despite the simulations sharing identical initial conditions and concentric isosurface structures. Furthermore, the study successfully reproduces the Ostwald ripening phenomenon, validating the system's tendency to minimize surface energy. We also confirm the strict preservation of the order parameter's boundedness within the physically admissible interval of $[-1, 1]$ throughout the evolution, ensuring both physical validity and numerical stability. These findings highlight the significant sensitivity of microstructural formation to domain-dependent parameters and demonstrate the robustness of the proposed numerical work.

1. INTRODUCTION

The Allen–Cahn (AC) equation, first introduced by Allen and Cahn [1], has long served as a model for anti-phase grain boundary coarsening and for understanding the motion of interfaces separating two distinct phases. It describes the evolution of two components in a binary alloy through a non-conserved Ginzburg–Landau functional, offering a simple representation of phase separation. Because of its analytical tractability and versatility, the AC equation has been widely adopted to model non-conservative phenomena in various disciplines, including biology, geometry [2], fluid mechanics, and image processing [3]. Numerous extensions and

Received November 28 2025; Revised December 12 2025; Accepted in revised form December 14 2025; Published online December 25 2025.

2020 *Mathematics Subject Classification.* 93B05.

Key words and phrases. Phase-Field equations, Allen–Cahn equation, Phase separation, Domain-dependent variable, Ginzburg–Landau equation.

[†] Corresponding author.

studies of AC–type equations have since been developed [4, 5, 6, 7, 8, 9], further broadening its impact across scientific research [10, 11, 12].

The AC equation has established itself as a fundamental framework across diverse scientific and engineering disciplines [13, 14]. In materials science, owing to its thermodynamic consistency, the equation is extensively employed within phase-field models to simulate microstructural evolution, such as solidification, thin film [15], grain growth [16, 17] and multi-components [18, 19]. Beyond its physical origins, the equation has found significant utility in computer vision and image processing, where it is applied to tasks such as image segmentation and denoising by treating image intensity as a phase-field [20, 3]. These diverse applications rely on the equation's capability to approximate motion by mean curvature [21, 22, 23], a property that necessitates robust numerical schemes capable of preserving physical characteristics such as the maximum principle and energy stability [15, 24, 25].

2. Discretization of the AC equation

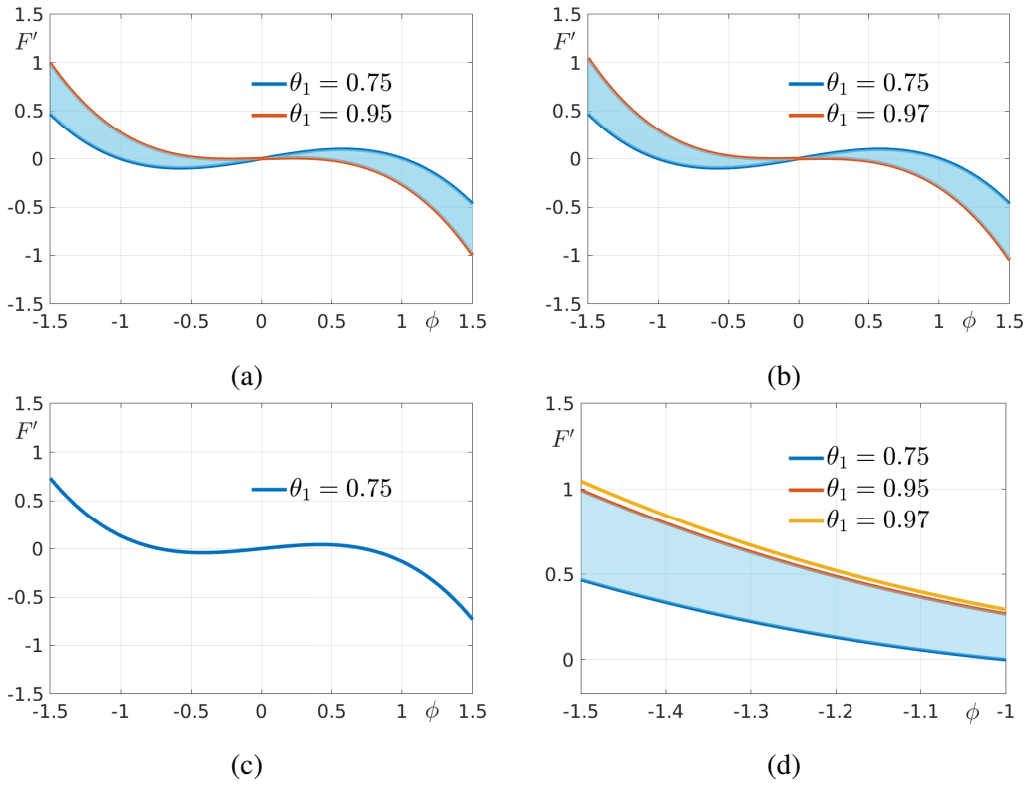

Figure 1: (a) $0.75 \leq \theta_1 \leq 0.95$, (b) $0.75 \leq \theta_1 \leq 0.97$, (c) $\theta_1 = 0.75$ and (d) close-up on $-1.5 \leq \phi \leq -1$.

In the AC equation, the logarithmic free-energy density is often adopted because it arises directly from mean-field or Flory–Huggins–type theories for binary mixtures, and therefore has a clearer thermodynamic interpretation than the classical double-well potential. Moreover, the logarithmic potential is singular at the pure phases, which naturally constrains the order parameter to stay within the physically admissible interval and improves the qualitative fidelity of the phase-field equation.

Figure 1 shows the variation of the quartic double-well potential F with respect to the temperature parameter θ_1, which approximates the logarithmic free energy to reflect the thermodynamic characteristics of the AC equation. With Fig. 1(a) serving as the reference, Fig. 1(c) represents the baseline case where θ_1 is fixed as a constant at 0.75. In contrast, Fig. 1(b) exhibits a value with a deviation of 0.02 from the maximum, indicating the fluctuation range of the potential curve induced by parameter changes. Finally, Fig. 1(d) presents a magnified close-up view of the specific region to clearly distinguish the subtle morphological differences among the potential curves shown in Fig. 1(a), (b), and (c).

Nevertheless, the logarithmic free energy can be used to capture the physical characteristics of phase separation, in this study we adopt a quartic double-well potential that effectively reflects the thermodynamic features implied by the logarithmic form. This choice allows us to retain the classical interpretation of the double-well potential while sufficiently incorporating its physical significance. We employ a quartic polynomial free energy functional effectively reflecting thermodynamic features [26]. The AC equation with the 4-th order polynomial potential can be written as

$$\frac{\partial \phi}{\partial t} = \epsilon \Delta_d \phi + \frac{1}{\epsilon}\left[(1-\theta_1)\phi - \frac{\theta_1}{3}\phi^3\right]. \tag{2.1}$$

In this equation, the parameter θ_1, representing the temperature T, plays a crucial role in the evolution.

For the numerical implementation, the AC equation (2.1) is discretized explicitly in time and space, which enables a straightforward evaluation of the approximate solution:

$$\begin{aligned}
\frac{\phi^{k+1}_{i,j,l} - \phi^k_{i,j,l}}{\Delta t} &= \epsilon \left(\frac{\phi^k_{i+1,j,l} + \phi^k_{i,j+1,l} + \phi^k_{i,j,l+1} + \phi^k_{i-1,j,l} + \phi^k_{i,j-1,l} + \phi^k_{i,j,l-1} - 6\phi^k_{i,j,l}}{h^2} \right) \\
&\quad + \frac{1}{\epsilon}\left[(1-\theta_{1,i,j,l})\phi^k_{i,j,l} - \frac{\theta_{1,i,j,l}}{3}(\phi^k_{i,j,l})^3\right], \\
\phi^{k+1}_{i,j,l} &= \frac{\epsilon \Delta t}{h^2}\left(\phi^k_{i+1,j,l} + \phi^k_{i,j+1,l} + \phi^k_{i,j,l+1} + \phi^k_{i-1,j,l} + \phi^k_{i,j-1,l} + \phi^k_{i,j,l-1}\right) \\
&\quad + \frac{\Delta t}{\epsilon}\left[\left(\frac{-6\epsilon^2}{h^2} + \frac{\epsilon}{\Delta t} + 1 - \theta_{1,i,j,l}\right)\phi^k_{i,j,l} - \frac{\theta_{1,i,j,l}}{3}(\phi^k_{i,j,l})^3\right].
\end{aligned}$$

Here, we describe the discrete domain Ω_h and discrete Laplacian operator. With a large $N \in \mathbb{N}$ and a uniform mesh grid size $h = 1/N$, the domain $\Omega = [0,1]^3 \subset \mathbb{R}^3$ is discretized by

$$\Omega_h = \{\mathbf{x}_{i,j,l} = ((i-1)h, (j-1)h, (l-1)h),\ 1 \le i,j,l \le N\}.$$

We denote $\phi(\mathbf{x}_{i,j,l}, k\Delta t)$ simply by $\phi^k_{i,j,l}$, where $\Delta t = \mathcal{T}/n_\mathcal{T}$ is a temporal step size with the final time $\mathcal{T}$ and the total number of temporal steps $n_\mathcal{T}$. We denote by ϕ^k the discrete solution at the k-th temporal step. We impose the zero Neumann boundary condition, i.e., $\frac{\partial \phi}{\partial \mathbf{n}} = 0$ on $\partial\Omega$, where $\mathbf{n}$ is the unit outward normal vector to the boundary $\partial\Omega$. In the discrete form, this condition is enforced by assuming the following values for the ghost points outside the domain. In a cell-corner grid, the discrete normal derivative at the boundary is approximated using a centered finite difference that involves one interior point and one ghost point. For example, on the left boundary, the discrete derivative in the x-direction is

$$\frac{\phi^k_{1,j,l} - \phi^k_{0,j,l}}{h} = 0,$$

that discrete derivative becomes zero for all $k > 0$. The same symmetric reflection is used for all boundaries:

$$\begin{aligned} \phi_{0,j,l} &= \phi_{1,j,l}, & \phi_{N+1,j,l} &= \phi_{N,j,l}, \\ \phi_{i,0,l} &= \phi_{i,1,l}, & \phi_{i,N+1,l} &= \phi_{i,N,l}, \\ \phi_{i,j,0} &= \phi_{i,j,1}, & \phi_{i,j,N+1} &= \phi_{i,j,N}, \end{aligned}$$

for $1 \le i, j, l \le N$. These conditions ensure that the discrete derivatives across the boundaries vanish.

The parameter ϵ is determined by the following relation:

$$\epsilon = \frac{4h}{2\sqrt{2}\tanh^{-1}(0.9)}.$$

The value of ϵ used in our equation follows a classical choice commonly employed in the classical AC equation [27]. The chosen ϵ does not come from a specific derivation or carry additional physical meaning in our setting. It is selected simply because it is a commonly used value in the classical AC literature, which helps us interpret the our equation without introducing unnecessary complexity.

3. NUMERICAL SIMULATIONS

This study focuses on observing key phase-field phenomena, including Ostwald ripening and the boundedness of the order parameter, within the numerical implementation of the AC equation. First, simulating Ostwald ripening is crucial because it validates the model's ability to accurately describe the evolution of non-uniform structures and phase coarsening. This process demonstrates the system's thermodynamic tendency to reduce total surface energy, where smaller particles with higher curvature dissolve and transfer material to larger particles. Successfully reproducing this phenomenon confirms that the model correctly captures the physical shift in size distribution as the average particle size increases over time.

Next, we see that boundedness of the order parameter. In classical AC equation, the order parameter is expected to remain in the interval $[-1, 1]$ to preserve physical meaning within a binary phase model and to remain compatible with the assumptions underlying the Ginzburg–Landau energy. Such a bound is also used analytically when employing maximum-principle

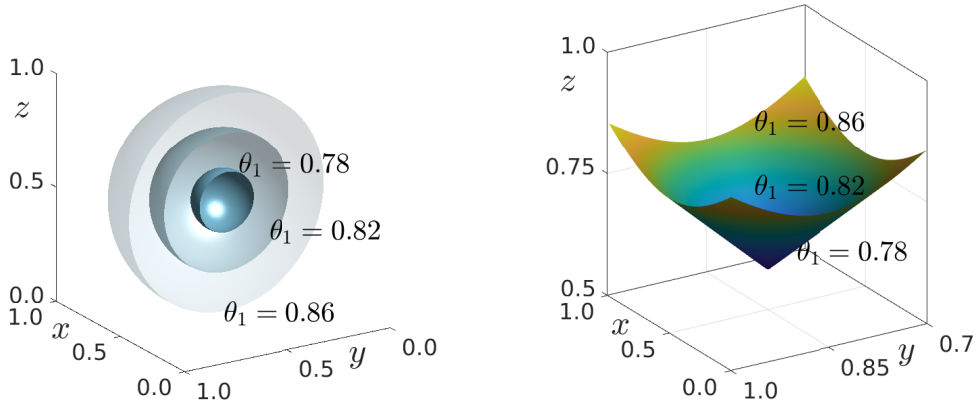

Figure 2: (a) shows the domain on which θ_1 is defined. The parameter θ_1 varies continuously from 0.75 to 0.95, and among the resulting concentric isosurfaces, only the levels 0.78, 0.82, and 0.86 are displayed. (b) presents the cross-sectional view obtained by slicing the unit-cube domain in (a) at $z = 0.5$, illustrating the function $\theta_1(x, y, 0.5)$.

arguments, proving well-posedness, or showing that diffuse interfaces converge to motion by mean curvature in the sharp-interface limit.

In our equation, however, the thermodynamically derived governing equation is used without any rescaling. As a result, the solution is not normalized, and it is not required to stay between -1 and 1. The classical boundedness condition is therefore unnecessary in our setting, and deviations from that range do not introduce inconsistencies or violate the structure of our free-energy form.

For all three cases, the simulations are initialized with the identical order parameter ϕ. While the parameter θ_1 varies for each case, we employ the same initial condition to ensure a direct comparison of the phase-field evolution. In addition, we set the initial values of ϕ to lie within the interval $[-1, 1]$. We perform numerical simulations for three cases depending on θ_1: (i) a variable range of $0.75 \leq \theta_1 \leq 0.95$, (ii) a wider variable range of $0.75 \leq \theta_1 \leq 0.97$, and (iii) a constant value of $\theta_1 = 0.85$. The difference in the upper bound between the first and second variable cases is 0.02. For the numerical parameters, we choose a time step size of $\Delta t = 0.125h^2$.

Figure 2(a) illustrates the spatial distribution of the temperature parameter θ_1 within the cubic domain, displaying concentric isosurfaces at values of 0.78, 0.82, and 0.86. This snapshot demonstrates the domain-dependent nature of the free energy, where the parameter varies radially from the center. Figure 2(b) depicts the corresponding surface profile of θ_1, highlighting the smooth, continuous gradient of the temperature field across the cross-section $z = 0.5$.

3.1. **Ostwald ripening.** Ostwald ripening is a phenomenon observed in solid or liquid solutions, describing how a non-uniform structure changes over time. It refers to the process where smaller particles or droplets gradually dissolve, and the dissolved material is transferred and deposited onto larger ones. This occurs because smaller particles, which have a higher curvature, are more soluble than larger particles with a lower curvature. As time passes, molecules from the smaller particles move through the surrounding medium and attach to the surfaces of larger particles. Since the system naturally tends to reduce its total surface energy, the smaller particles keep shrinking and may eventually disappear, while the larger particles grow. As a result, the average particle size increases, and the overall size distribution shifts toward larger values.

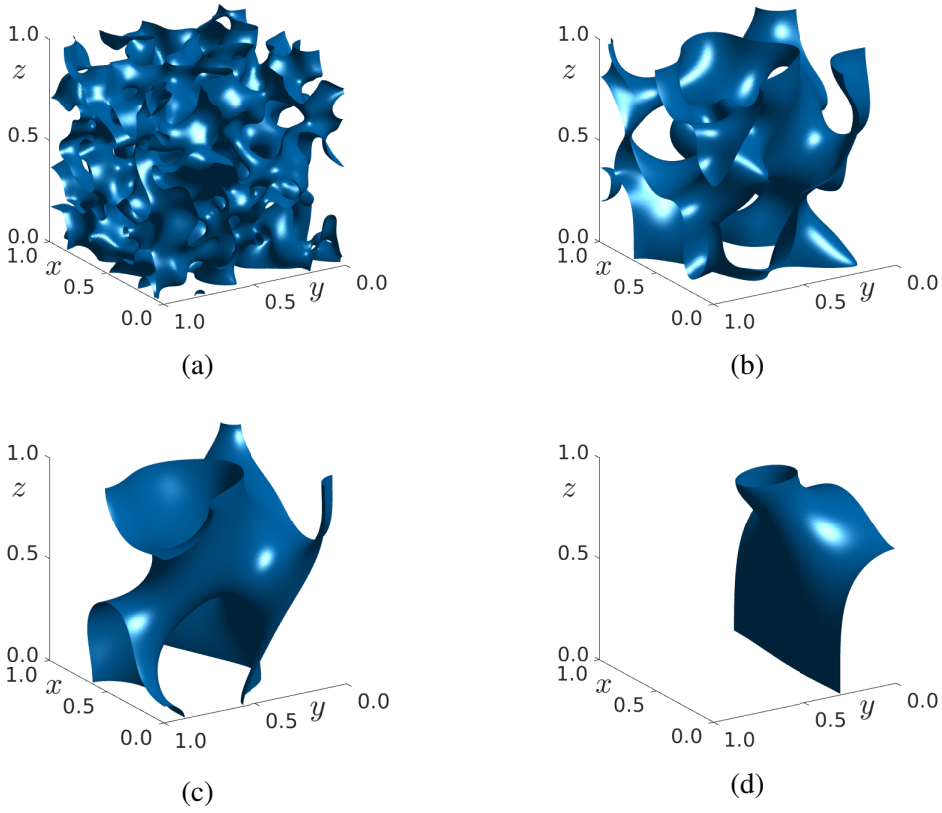

Figure 3: $0.75 \leq \theta_1 \leq 0.95$. (a) $T = 0$, (b) $T = 120000 \times \Delta t$, (c) $T = 400000 \times \Delta t$ and (d) $T = 1560000 \times \Delta t$.

As we can see the Figure 3 in this simulation with a domain-dependent θ_1, the coarsening effect characteristic of phase-field models is clearly observed. As time progresses, the phases

gradually coalesce, and the system eventually converges to a trivial solution in the form of a planar interface.

Figure 3(a) presents the three-dimensional initial condition generated in the domain $\Omega = [0,1] \times [0,1] \times [0,1]$ using a random-structured field distribution. Starting from a disordered state with random noise, the order parameter forms a spatially entangled interface structure as shown by the blue isosurface at $\phi = 0$. This topology exhibits a bicontinuous, sponge-like morphology where the two phases are intimately mutually connected. Such a structure serves as an ideal test bed for observing phase-field dynamics, as the system is poised to undergo surface energy minimization, leading to the rapid smoothing of interfaces and the subsequent Ostwald ripening process.

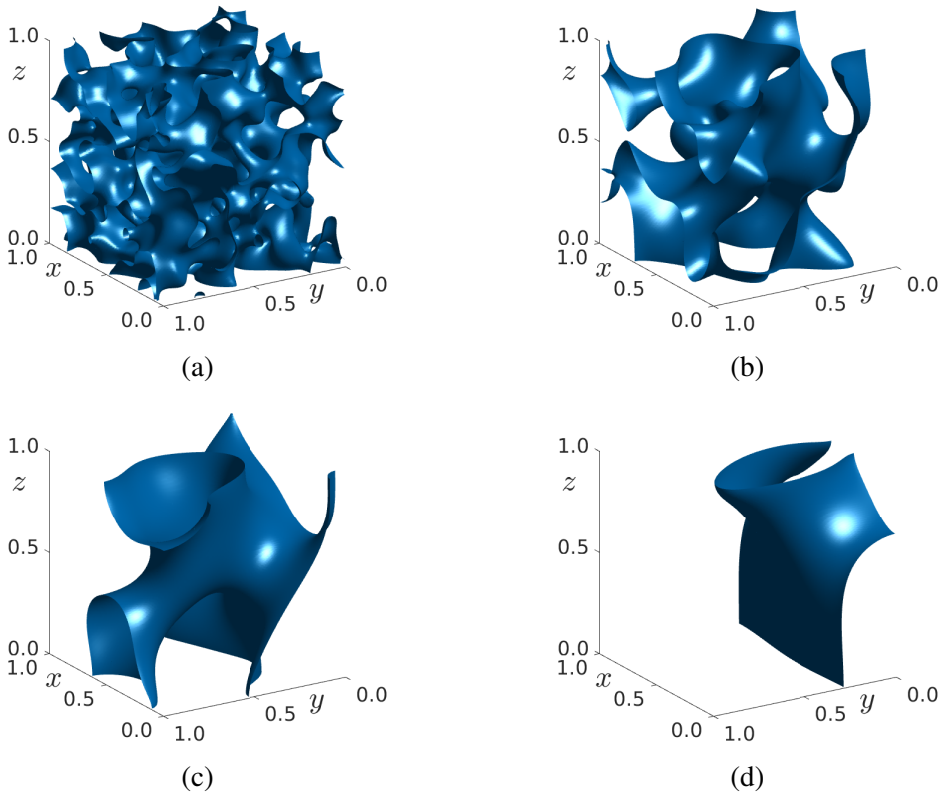

Figure 4: $0.75 \leq \theta_1 \leq 0.97$. (a) $T = 0$, (b) $T = 120000 \times \Delta t$, (c) $T = 400000 \times \Delta t$ and (d) $T = 1560000 \times \Delta t$.

Figure 4, compared to the first case, the second simulation has a maximum θ_1 value that differs by a relatively small margin of 0.02. Although both cases share the identical initial condition for ϕ and the same concentric isosurface structure for θ_1, they differ merely by this

magnitude. Remarkably, this slight numerical deviation leads to a distinct topological change in the final state of the simulation, as seen in Fig. 4(d).

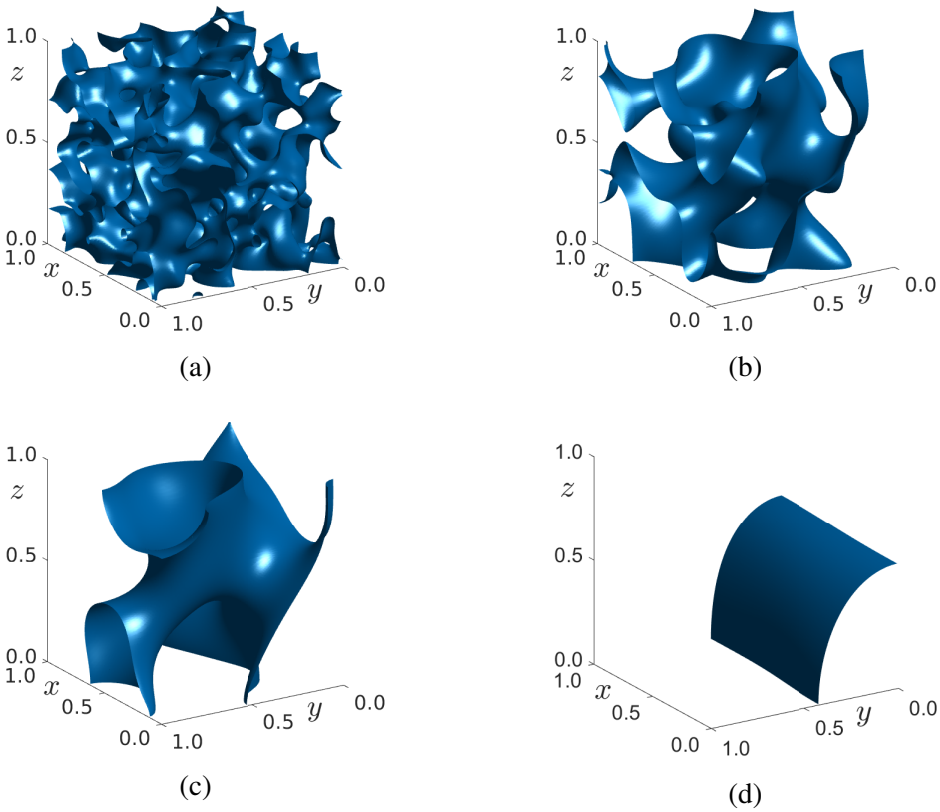

Figure 5: $\theta_1 = 0.85$. (a) $T = 0$, (b) $T = 120000 \times \Delta t$, (c) $T = 400000 \times \Delta t$ and (d) $T = 1560000 \times \Delta t$.

The third simulation in Fig. 5 corresponds to the conventional AC equation where θ_1 is held constant. Although it shares the identical initial condition with the previous two cases, it exhibits distinct differences in topological changes during its evolution.

The blue, red, and yellow surfaces in Fig. 6 correspond to the first, second, and third cases, respectively. The light gray surface represents the isosurface where $\theta_1 = 0.85$.

3.2. **Boundedness of an order parameter.** In the AC equation, the order parameter represents two distinct phases and is typically associated with the minima of a double-well potential located at -1 and $+1$. For this reason, it is important that the solution remain within the interval $[-1, 1]$]. Values outside this range would have no clear physical interpretation in the binary-phase setting and would break the assumptions built into the model. This restriction

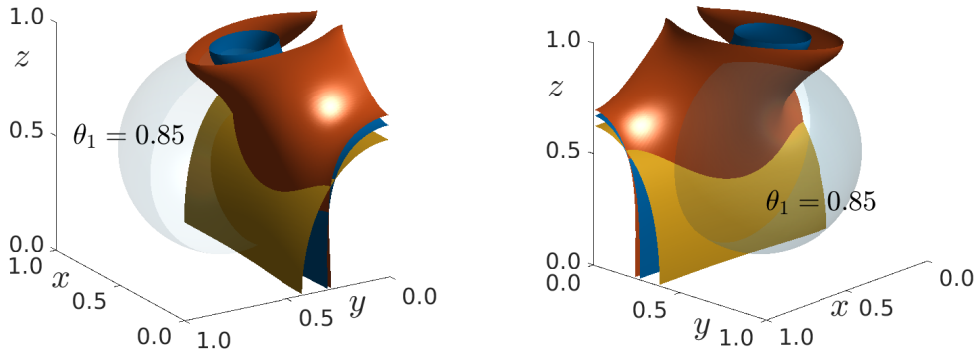

Figure 6: Overlapped results of the final evolution for the three cases. The results are displayed from different viewpoints: (a) is observed from $x = 0, y = 1$, and (b) from $x = 1, y = 1$.

also serves an essential mathematical purpose: it allows the use of maximum-principle arguments, stabilizes the nonlinear terms arising from the potential, and is frequently required in analyses concerning existence, uniqueness, and regularity of solutions.

Staying within $[-1, 1]$ is equally significant for the energy structure of the equation. The Ginzburg–Landau energy is shaped around wells at ± 1, and solutions that remain in this interval correctly follow the intended energy landscape, staying near the wells except within thin transition layers. This property is also crucial in the sharp-interface limit $\epsilon \to 0$; only when the solution stays inside the physical range do the transition layers converge to interfaces moving by mean curvature in the standard way.

From a computational perspective, keeping numerical solutions inside $[-1, 1]$ helps avoid nonphysical oscillations and greatly improves stability. Many effective numerical schemes therefore incorporate techniques that preserve this range at the discrete level, leading to more reliable long-time simulations and more accurate representation of metastable patterns. In summary, requiring the solution to stay in $[-1, 1]$ is vital for physical interpretation, analytical arguments, asymptotic behavior, and numerical robustness.

In all three cases, small phase bulks shrink rapidly over time, while relatively larger ones diminish at a much slower rate. This disparity leads to fluctuations in the maximum and minimum values of the order parameter, as seen in Fig. 7. Nevertheless, the theoretical bounds are strictly preserved throughout the process.

4. Conclusion

In this study, we have presented a comprehensive numerical investigation of the Allen–Cahn equation characterized by a domain-dependent free energy functional. By adopting a quartic

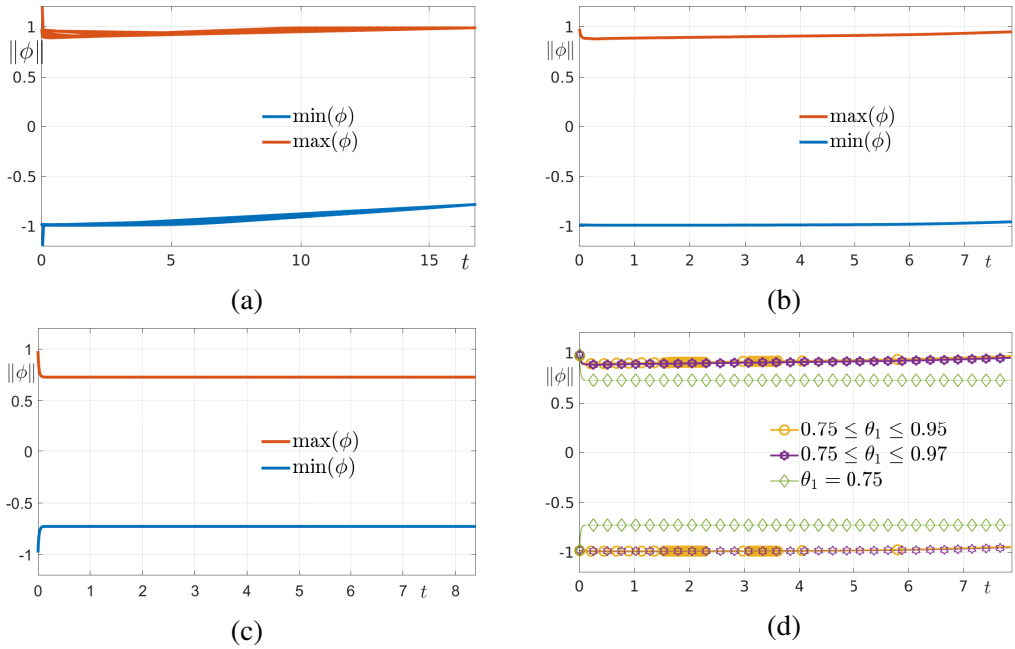

Figure 7: (a) $0.75 \leq \theta_1 \leq 0.95$, (b) $0.75 \leq \theta_1 \leq 0.97$, (c) $\theta_1 = 0.75$ and (d) The overlapped graphs demonstrate the boundedness of the order parameter.

polynomial potential to approximate the logarithmic free energy, we established a model that effectively captures the thermodynamic features of phase separation while maintaining analytical tractability.

The primary objective was to analyze the morphological evolution of the phase field under spatially varying temperature parameters, θ_1, and to verify the physical and mathematical consistency of the numerical scheme.Our three-dimensional simulations yielded several significant insights into the dynamics of the phase-field model. First, we successfully demonstrated the phenomenon of Ostwald ripening within the domain-dependent evolutions. The simulation results clearly showed the dissolution of smaller phase bulks with higher curvature and the consequent growth of larger domains, validating the system's thermodynamic tendency to minimize total surface energy and eventually converge to a trivial planar interface.

Second, we confirmed the boundedness of the order parameter, a critical requirement for both physical interpretation and numerical stability. Despite the rapid shrinking of small bulks causing fluctuations in the extrema, the solution remained strictly preserved within the physically admissible interval of $[-1, 1]$ throughout the evolution. This preservation is essential for satisfying the maximum principle and ensuring the energy consistency of the Ginzburg-Landau functional. Most notably, the comparative analysis of three distinct scenarios revealed the high sensitivity of the topological evolution to the spatial distribution of the temperature

parameter. Although the simulations were initialized with identical order parameter configurations and shared the same concentric isosurface structures for θ_1, a marginal difference of 0.02 in the maximum value of the variable parameter resulted in distinctly different final topological states. This finding highlights that even subtle variations in domain-dependent parameters can induce significant divergence in microstructural formation compared to the conventional constant-parameter model. In conclusion, this work verifies that the proposed numerical framework is robust and capable of simulating complex phase-field dynamics, offering valuable insights into the impact of non-uniform energy potentials on material evolution.

ACKNOWLEDGMENTS

This work was supported by the National Research Foundation of Korea (NRF) (RS-2025-24523064).

REFERENCES

[1] S. M. Allen and J. W. Cahn, *A microscopic theory for antiphase boundary motion and its application to antiphase domain coarsening*, Acta Metallurgica, **27** (1979), 1085–1097.
[2] D. Lee, *Computing the area-minimizing surface by the Allen–Cahn equation with the fixed boundary* , AIMS math., **8**(10) (2023), 23352–23371.
[3] D. Lee and S. Lee, *Image segmentation based on modified fractional Allen–Cahn Equation*, Math. Probl. Eng., **2019** (2019), 3980181.
[4] D. Lee, *The numerical solutions for the energy-dissipative and mass-conservative Allen–Cahn equation*, Comput. Math. Appl, **80**(1) (2020), 263–284.
[5] D. Lee, *Gradient-descent-like scheme for the Allen–Cahn equation*, AIP Adv., **13**(8) (2023), 085010.
[6] D. Lee and J. Kim, *Comparison study of the conservative Allen–Cahn and the Cahn–Hilliard equations*, Math. Comput. Simul, **119** (2016), 35–56.
[7] D. Lee and Y. Kim, *Novel mass-conserving Allen–Cahn equation for the boundedness of an order parameter*, Commun. Nonlinear Sci. Numer. Simul., **85** (2020), 105224.
[8] D. Lee and C. Lee, *Numerical solutions of the Allen–Cahn equation with the p-Laplacian*, Appl. Math. Comput., **434** (2022), 127435.
[9] S. Lee and D. Lee, *The fractional Allen–Cahn equation with the sextic potential*, Appl. Math. Comput., **351**(15) (2019), 176–192.
[10] Q. Du and R. A. Nicolaides, *Numerical analysis of a continuum model of phase transition*, SIAM Journal on Numerical Analysis, **28** (1991), 1310–1322.
[11] D.J. Eyre, *Unconditionally gradient stable time marching the Cahn–Hilliard equation*, MRS Online Proceedings Library, **529** (1998), 39–46.
[12] D. Lee and C. Lee, *Assessment of morphological similarities for the conservative Allen–Cahn and Cahn–Hilliard equations*, J. Comput. Sci., **76** (2024), 102240.
[13] C. Lee, Y. Choi and J. Kim, *An explicit stable finite difference method for the Allen–Cahn equation*, Appl. Numer. Math., **182** (2022), 87–99.
[14] D. Lee and H. Kim, *The time-fractional Allen–Cahn equation on geometric computational domains*, Commun. Nonlinear Sci. Numer. Simul., **141** (2025), 108455.
[15] D. Li, Z. Qiao and T. Tang, *Gradient bounds for a thin film epitaxy equation*, Journal of Differential Equations, **262** (2017), 1720–1746.
[16] L. Q. Chen, *Phase-field models for microstructure evolution*, Annual Review of Materials Research, **32** (2002), 113–140.

[17] O. Penrose and P. C. Fife, *Thermodynamically consistent models of phase-field type for the kinetics of phase transitions*, Physica D: Nonlinear Phenomena, **43** (1990), 44–62.
[18] C. M. Elliott and S. Luckhaus, *A generalized diffusion equation for phase separation of a multi-component mixture with interfacial free energy*, SFB 256 Preprint, University of Bonn, (1991).
[19] H. Lee, J. Lee and J. Shin, *A constrained convex splitting scheme for the vector-valued Cahn–Hilliard equation*, J. KSIAM, **23**(1) (2019), 1–18.
[20] G. Aubert and P. Kornprobst, *Mathematical problems in image processing*, Applied mathematical sciences 147, Springer Verlag, New York, 2002.
[21] L. C. Evans, H. M. Soner and P. E. Souganidis, *Phase transitions and generalized motion by mean curvature*, Communications on Pure and Applied Mathematics, **45** (1992), 1097–1123.
[22] D. Gil and P. Radeva, *Curvature vector flow to assure convergent deformable models for shape modeling*, Lecture Notes in Computer Science, Springer Verlag, Proceedings of EMMCVPR, Lisbon, Portugal 2003.
[23] J. Yang, S. Kang, S. Kwak and J. Kim, *The Allen–Cahn equation with a space-dependent mobility and a source term for general motion by mean curvature*, J. Comput. Sci., **77** (2024), 102252.
[24] J. Shen and X. Yang, *Numerical approximations of Allen–Cahn and Cahn–Hilliard equations*, Discrete & Continuous Dynamical Systems-A, **28** (2010), 1669–1691.
[25] T. Tang and J. Yang, *Implicit-explicit scheme for the Allen–Cahn equation preserves the maximum principle*, Journal of Computational Mathematics, **34** (2016), 471–481.
[26] Y. Kim and D. Lee, *Numerical investigation into the dependence of the Allen–Cahn equation on the free energy*, Adv. Comput. Math., **48** (2022), 36.
[27] D. Lee, J. Huh, D. Jeong, J. Shin, A. Yun and J. Kim, *Physical, mathematical, and numerical derivations of the Cahn–Hilliard equation*, Comput. Mater. Sci., **81** (2014), 216–225.